Supplementary Information for

Strong and tunable spin-orbit interaction in a single crystalline InSb nanosheet

Yuanjie Chen[1], Shaoyun Huang[1], Dong Pan[2], Jianhong Xue[1], Li Zhang[1], Jianhua Zhao[2,3,*], and H. Q. Xu[1,3,†]

[1]*Beijing Key Laboratory of Quantum Devices, Key Laboratory for the Physics and Chemistry of Nanodevices and Department of Electronics, Peking University, Beijing 100871, China*

[2]*State Key Laboratory of Superlattices and Microstructures, Institute of Semiconductors, Chinese Academy of Sciences, P.O. Box 912, Beijing 100083, China*

[3]*Beijing Academy of Quantum Information Sciences, Beijing 100193, China*

Corresponding authors. Emails: [†]hqxu@pku.edu.cn; [*]jhzhao@semi.ac.cn

(Dated: November 16, 2020)

Supplementary Note I. Determination of the carrier density and carrier mobility in the InSb nanosheet

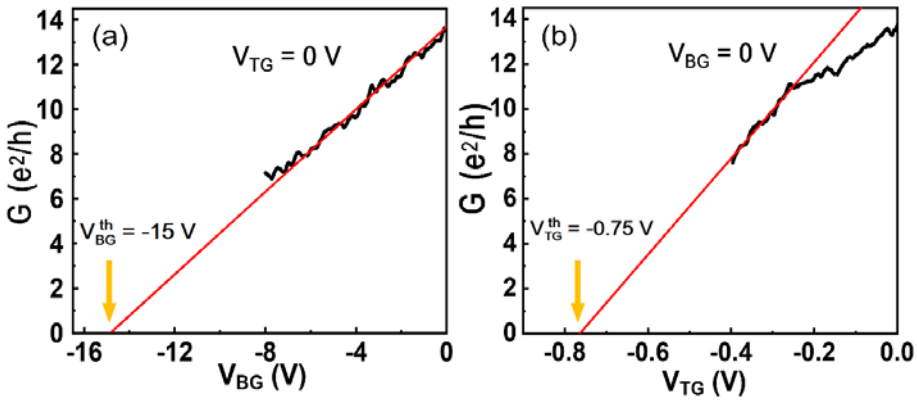

Figure 1. (a) Conductance *G* (black line) measured for the InSb nanosheet in the dual-gate device as a function of back gate voltage V_{BG} at top gate voltage V_{TG} = 0 V and at *T* = 1.9 K. The red line is a linear fit to the measurements. This fitting line is extended to intersect the back-gate axis at which the back gate threshold voltage $V_{\mathrm{BG}}^{\mathrm{th}} = -15$ V (as marked by a yellow arrow) is extracted. (b) Conductance *G* (black line) measured for the InSb nanosheet in the dual-gate device as a function of top gate voltage V_{TG} at bottom gate voltage V_{BG} = 0 V and at *T* = 1.9 K. The red line is a linear fit to the measurements. This fitting line is extended to intersect the top-gate axis at which the top gate threshold voltage $V_{\mathrm{TG}}^{\mathrm{th}} = -0.75$ V (as marked by a yellow arrow) is extracted.

In this Supplementary Note, we describe how the carrier density and carrier mobility in the InSb nanosheet of the dual-gate device are extracted from the measured gate transfer characteristics of the device. Figure 1(a) shows the conductance of the nanosheet measured at T = 1.9 K as a function of the back gate voltage V_{BG} (back gate transfer characteristics) with top gate voltage fixed at V_{TG} = 0 V. The measurements are carried out in a four-probe configuration (see Fig. 1a in the main article for the measurements circuit setup), in which a 17 Hz AC excitation current I of 100 nA is applied through the two outer electrodes and the voltage drop V between the two inner electrodes is reordered. Because the effect of the contact resistances has been eliminated in such four-probe measurements, the conductance of the nanosheet can be obtained directly from $G = I/V$. The carrier density in the nanosheet can be estimated from $n = C_{\mathrm{gs}} \times \frac{V_{\mathrm{BG}} - V_{\mathrm{BG}}^{\mathrm{th}}}{e}$, where C_{gs} is the unit area capacitance of the back gate and $V_{\mathrm{BG}}^{\mathrm{th}}$ is the back gate threshold voltage at which the conductance of the nanosheet goes to zero. Here we estimate C_{gs} using a parallel capacitor model $C_{\mathrm{gs}} = \frac{\varepsilon\varepsilon_0}{d}$, where ε_0 is the vacuum permittivity, ε and d are the dielectric constant and thickness of the gate dielectric. Using ε = 3.9 and d = 300 nm for the dielectric layer of SiO_2 in this work, we obtain $C_{\mathrm{gs}} = 1.15 \times 10^{-8}$ F $\cdot$ cm^{-2}. The back gate threshold voltage $V_{\mathrm{BG}}^{\mathrm{th}}$ is extracted from the measured back-gate transfer characteristics shown in Fig. 1(a) as follows. First, we fit the measured back-gate transfer characteristics by a line (red line in the figure). Then, we extend the fitting line to intersect the back-gate voltage axis and the back gate value at the intercept is the extracted value for $V_{\mathrm{BG}}^{\mathrm{th}}$. From the measurements shown in Fig. 1(a), $V_{\mathrm{BG}}^{\mathrm{th}} \sim -15$ V is obtained. The carrier density in the nanosheet can now be evaluated at a given value of V_{BG}. For example, at $V_{\mathrm{BG}} = -5$ V (corresponding to a case with the nanosheet channel conductance of $G \sim 9\,e^2/h$), a carrier density of n = 7.2×10^{11} cm^{-2} in the nanosheet is obtained, while at $V_{\mathrm{BG}} = -9$ V (corresponding to a case with the nanosheet channel conductance of $G \sim 5\,e^2/h$), a carrier density of n = 4.3×10^{11} cm^{-2} in the nanosheet is obtained.

The carrier mobility in the InSb nanosheet can be obtained from $\mu = \sigma/ne$, where $\sigma = \frac{GL}{W}$ is the nanosheet channel conductivity with L being the channel length (i.e., the distance between the two inner contacts, about 1.1 μm in this device) and W the channel width (i.e., the width of the nanosheet, about 550 nm in this device). Here, we note that since both the nanosheet conductance and the carrier density in the

nanosheet depend linearly on V_{BG}, the extracted carrier mobility from the transfer characteristic measurements (which is often called the field effect mobility) will be independent of V_{BG}. Thus, we can evaluate the carrier mobility μ by setting the back gate voltage value at, e.g., $V_{\mathrm{BG}} = -5$ V, at which the carrier density is $n = 7.2 \times 10^{11}$ cm^{-2} and the nanosheet conductance is $G \sim 9e^2/h$. The obtained carrier mobility is then $\mu \sim 6000$ cm$^2 \cdot$V$^{-1} \cdot$s^{-1}. The carrier mean free path in the nanosheet is given by $L_{\mathrm{e}} = \frac{\hbar\mu}{e}\sqrt{2\pi n}$, where $\hbar = \frac{h}{2\pi}$ with h being the Planck constant. From the measured back gate transfer characteristics shown in Fig. 1(a), we obtain $L_{\mathrm{e}} \sim$ 84 nm at $n = 7.2 \times 10^{11}$ cm^{-2} (and $G \sim 9e^2/h$) and $L_{\mathrm{e}} \sim$ 65 nm at $n = 4.3 \times 10^{11}$ cm^{-2} (and $G \sim 5e^2/h$).

Using the top-gate transfer characteristics shown in Fig. 1(e), similar results for the carrier density and electron mobility in the InSb nanosheet should be extracted. However, since the dielectric constant of HfO_2 in our device is an unknown parameter, which has been given to over a wide range of values in the literature, a direct estimation of the carrier density and electron mobility in the InSb nanosheet from the top-gate transfer characteristics is not possible. Nevertheless, using the results obtained above, we can determine the dielectric constant of HfO_2 employed in our device. The equation to be used for extraction of the carrier density based on the top-gate transfer characteristics becomes $n = C_{\mathrm{gs}} \times \frac{V_{\mathrm{TG}} - V_{\mathrm{TG}}^{\mathrm{th}}}{e}$, where $C_{\mathrm{gs}} = \frac{\varepsilon\varepsilon_0}{d}$ with ε being the unknown dielectric constant of HfO_2, d = 20 nm the thickness of HfO_2, and $V_{\mathrm{TG}}^{\mathrm{th}}$ the top-gate threshold voltage at which the conductance G goes to zero. Similarly as in Fig. 1(a), $V_{\mathrm{TG}}^{\mathrm{th}}$ can be extracted from the measurements shown in Fig. 1(b) by a linear fit to the low top-gate voltage data and by extending the fitting line to intersect the top-gate voltage axis. As seen in Fig. 1(b), a result of $V_{\mathrm{TG}}^{\mathrm{th}} \sim -0.75$ V is obtained. To determine the dielectric constant ε of HfO_2 in our device, we consider the case of the conductance $G \sim 9e^2/h$ at $V_{\mathrm{TG}} = -0.35$ V, corresponding to the case of carrier density $n = 7.2 \times 10^{11}$ cm^{-2} as estimated through the bottom-gate transfer characteristics. By taking this value into the above equation, a value of $\varepsilon \sim 6.5$ can be obtained for the dielectric constant of HfO_2 in our device. This value indicates that the HfO_2 layer in our device is in good amorphous phase, consistent with the fact that it was grown at a low temperature by atomic layer deposition.

Supplementary Note II. Comparison between the results obtained by analyses of magnetotransport measurements of the InSb nanosheet using the HLN and ILP theories

In the main article, the HLN model is utilized in the analysis of our magnetotransport data. This is suitable for a weak disordered system such as InSb nanosheet and other emerging 2D materials, where the electron elastic scattering length, or the mean free path, L_{e} is shorter than all other characteristic transport length scales, such as phase coherence length L_{φ} and spin-orbit length L_{SO}. However, in a clean 2D electron system with a ultrahigh mobility made from a semiconductor heterostructured quantum well, L_{e} can be exceedingly longer than L_{SO}. In this case, the HLN model may no longer be applicable and one might need to invoke the so-called ILP model, developed by Iordanskii, Lyanda-Geller and Pikus[1], in analyses of the magnetotransport measurement data. Here, it is worthwhile to check whether the ILP model can be applied to the magnetotransport data obtained in our device. In the ILP model, the quantum conductance correction to the low-field magnetoconductance is given by

$$\Delta\sigma_{\mathrm{ILP}} = -\frac{e^2}{4\pi^2\hbar}\left\{\frac{1}{a_0} + \frac{2a_0+1+\frac{H_{\mathrm{SO}}}{B}}{a_1\left[a_0+\frac{H_{\mathrm{SO}}}{B}\right]-2\frac{H'_{\mathrm{SO}}}{B}} + 2\ln\frac{H_{\mathrm{tr}}}{B} + \psi\left(\frac{1}{2}+\frac{H_{\varphi}}{B}\right) + 3C - \sum_{n=1}^{\infty}\left[\frac{3}{n} - \frac{3a_n^2+2a_n\frac{H_{\mathrm{SO}}}{B}-1-2(2n+1)\frac{H'_{\mathrm{SO}}}{B}}{\left[a_n+\frac{H_{\mathrm{SO}}}{B}\right]a_{n-1}a_{n+1}-2\frac{H'_{\mathrm{SO}}}{B}[(2n+1)a_n-1]}\right]\right\}. \quad (1)$$

Here, $H_{\mathrm{SO}} = H'_{\mathrm{SO}} + H^3_{\mathrm{SO}}$ with H'_{SO} being Rashba term and $H^3_{\mathrm{SO}} > 0$ the cubic Dresselhaus term, $a_n = n + \frac{1}{2} + \frac{H_{\varphi}}{B} + \frac{H_{\mathrm{SO}}}{B}$, C is Euler's constant, $H_{\mathrm{tr}} = \frac{\hbar}{4eL_{\mathrm{e}}^2}$, and $H_{\varphi} = \frac{\hbar}{4eL_{\varphi}^2}$. In the calculations using the above equation, the summation of first 10000 terms in the series has been performed and it is checked that a desired convergence has been achieved.

Figure 2 given below shows a comparison between the results of analyses using the HLN and ILP theories, where the magnetoconductance data (dots) measured for our InSb nanosheet device at T = 1.9 K, V_{TG} = −0.46 V and V_{BG} = 1.54 V, and the best fits to the data by both the HLN (light blue line) and ILP (light green line) models are presented. Clearly, the HLN model yields a satisfactory fit to the measurement data, giving the extracted length scales of L_{φ}= 472 nm, L_{SO}=137 nm and L_{e}= 88 nm. However, large deviations from the measurements are found in the best fit to the ILP model. In addition, the best fit by the ILP model gives H'_{so}= 4.35×10^{-2} T, H_{φ}=

4.04×10^{-4} T, H_{tr}= 2.98×10^{-2} T, and H_{so}^{3}= 6.2×10^{-21} T ($\approx$0 T), and thus the length scales of L_{φ}= 638 nm , L_{SO}= 61 nm and L_{e} = 74 nm. Here, both the values of L_{φ} and L_{e} may look reasonable , but the value of $L_{\mathrm{so}}(< L_{\mathrm{e}})$ looks unphysical for the InSb nanosheet in our device. Thus, for our InSb nanosheet device, it is more appropriate to use the HLN model, instead of the ILP model, for analyses of our measured magnetoconductance data.

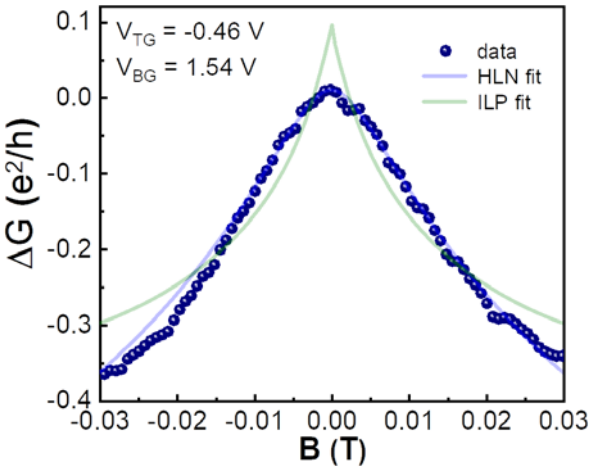

Figure 2. Comparison between the best fits of the magnetoconductance data measured for our InSb nanosheet device at T = 1.9 K, V_{TG} = −0.46 V and V_{BG} = 1.54 V to the HLN and ILP models.

Supplementary Note III. Materials parameters and simulations for energy band diagrams

To simulate the energy band diagrams of the HfO_2-InSb-SiO_2 structure in the dual-gate InSb nanosheet device, Poisson's equation is solved using commercially available program COMSOL in compliance with the boundary conditions set in our experiment. Here we assume that each material layer is an infinite two-dimensional structure and we thus need to solve effectively only a one-dimensional Poisson's equation. Material parameters of InSb, SiO_2 and HfO_2 utilized in the simulations for the energy band diagrams are given in Table I.

Poisson's equation used here to describe the electrostatics of the HfO_2-InSb-SiO_2 heterostructure has a form of

$$\nabla\cdot(-\epsilon_{\mathrm{r}}\nabla V)=q(p-n+N_{\mathrm{d}}^{+}-N_{\mathrm{a}}^{-}), \qquad (2)$$

where V is the electric potential, ϵ_{r} is the dieletric constant of the material, q is the

elementary charge, p and n are the hole and electron densities, N_{d}^{+} and N_{a}^{-} are the ionized donor and acceptor concentrations, respectively. The energies of the conduction and valence band edges can be calculated as, $E_{\mathrm{c}} = -(eV + \chi_0)$ and $E_{\mathrm{V}} = -(eV + \chi_0 + E_{\mathrm{g},0})$, where χ_0 and $E_{\mathrm{g},0}$ are the electron affinity and bandgap of a material. The continuity conditions at the interface of two different materials are, $\boldsymbol{n} \cdot (D_1 - D_2) = 0$ and $E_{\mathrm{F},1} = E_{\mathrm{F},2}$, where $\boldsymbol{n}$ denotes the normal vector of the interface, $D_{1,2}$ and $E_{\mathrm{F},1,2}$ are the electric displacements and electron Fermi levels in the two materials.

Table I. Material parameters of InSb, SiO_2 and HfO_2 utilized in the simulations for the HfO_2-InSb-SiO_2 heterostructure in the dual-gate InSb nanosheet device at $T = 2$ K.

Material	Bandgap (eV)	Dielectric Constant	Electron Effective Mass (m_0)	Electron Affinity (eV)
InSb	0.23[1]	16.8	0.014	4.77[2]
HfO_2	5.8	6.5[3]	0.11	2.8[4]
SiO_2	8.95	3.9	0.3	0.75[5]

[1] Littler, C. L. & Seiler, D. G. *Appl. Phys. Lett.* **46**, 986 (1985).

[2] Freeouf, J. L., and J. M. Woodall. *Appl. Phys. Lett.* **39**, 727-729 (1981).

[3] From this work.

[4] Sayan, S., Eric Garfunkel, and S. Suzer. *Appl. Phys. Lett.* **80**, 2135-2137 (2002).

[5] Fujimura, Nobuyuki, et al. *Japanese Journal of Applied Physics* **55.** 08PC06 (2016)

Figure 3(a) is the zoom-in figure of Fig. 4b in the main article which displays the calculated profiles of the conduction band edge inside the InSb layer at the experimental condition of the carrier density n =7.2×10^{11} cm^{-2} and the conductance G ~$9e^2/h$ with three different values of voltage V_{D} applied over the dual gate. Clearly the conduction band edge inside the InSb layer is bended, leading to the presence of an electric field in the layer. Figure 3(b) shows the calculated electric field distribution inside the InSb layer at the three considered values of V_{D}. Clearly, among the three cases, an overall strongest field strength is found inside the InSb layer for V_{D} = −2 V, which should give a strong SOI. On the contrast, at V_{D} = 11 V, the field strength inside the InSb layer is overall small, which should produce a relatively weak SOI. Figure 3(c) displays the calculated carrier density distributions in the InSb layer at the three values of V_{D}. As shown in Fig. 3(c), at V_{D} = −2 and 0 V, carriers are non-uniformly distributed and they mainly concentrated to the bottom part of the InSb layer, close to the SiO_2 dielectric, where strong electric fields are presented and carriers will experience a

strong Rashba SOI when they move along the layer. At V_D = 11 V, the carrier distribution becomes less non-uniform in the InSb layer with a significant amount appearing in the middle region of the layer, where the electric field is comparably weak and the carriers would experience a weak SOI in the InSb nanosheet. All these simulated results are in a good agreement with our experimentally measured results for the SOI in the InSb nanosheet.

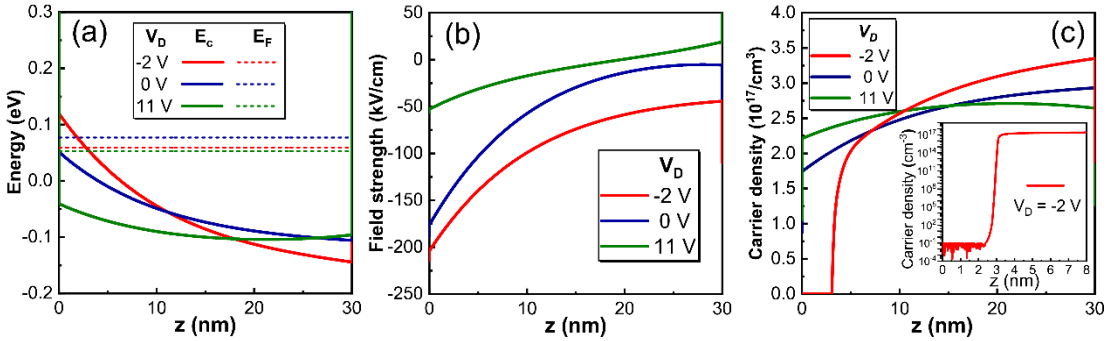

Figure 3. (a) Calculated conduction band edges (red, blue and green solid lines) and Fermi levels (red, blue and green dashed lines) inside the InSb layer with a sheet carrier density $n = 7.2 \times 10^{11}$ cm^{-2} at three different values of dual-gate voltage V_D. (b) Calculated corresponding effective electric field strengths inside the InSb layer at the same three values of V_D as in (a). (c) Calculated corresponding carrier density distributions inside the InSb layer at the same three values of V_D as in (a). The inset shows the results of the calculations at $V_D = -2$ V with the carrier density plotted in logarithmic scale.

Supplementary Note IV. Analysis of the Rashba SOI in the InSb nanosheeet

In a semiconductor quantum structure, two predominant mechanisms that give rise to spin-orbit coupling and thus lift the spin degeneracy even in the absence of a magnetic field are the Dresselhaus and Rashba[2] SOI. The first one arises from an intrinsic bulk inversion asymmetry (BIA) of the underlying crystal structure, as described by Dresselhaus[3], while the second one arises from a structural inversion asymmetry (SIA) induced by an electrical field $\mathbf{E} = -\nabla V(\mathbf{r})$ in the crystal, where $V(\mathbf{r})$ is the electric potential, as described by Bychkov and Rashba[4]. The electric field could include both a built-in part in the structure and a tunable part created by, e.g., applying a gate voltage.

In the lowest-order approximation, the Rashba SOI Hamiltonian can be written as[5]

$$H_{\mathrm{R}} = r_{\mathrm{R}}\boldsymbol{\sigma} \cdot \mathbf{k} \times \mathbf{E}, \quad (3)$$

where r_{R} is a material-specific, Fermi level dependent prefactor[6,7] and $\mathbf{k}$ is the wave vector. To estimate the effect of the Rashba SOI in our dual-gate device structure, we assume that all conduction carriers experience a same electric field in the InSb nanolayer. We approximate this electric field by the mean electric field $\mathbf{E} = (0,\ 0,\ E)$, with E being the perpendicular component of the electrical field obtained by averaging through the InSb nanolayer along the perpendicular direction. The wave vector only has in-plane components and can be written as $\mathbf{k} = (k_x, k_y, 0)$. Rashba Hamiltonian then becomes $H_{\mathrm{R}} = \alpha_{\mathrm{R}}(k_y\sigma_x - k_x\sigma_y)$, where $\alpha_{\mathrm{R}} = r_{\mathrm{R}}E$ is known as the Rashba SOI strength parameter. Moreover, the spin-orbit precession length is given by $L_{\mathrm{R}} = \frac{\hbar^2}{m^*\alpha_{\mathrm{R}}}$ with m^* being the elecron effective mass. Therefore $\frac{1}{L_{\mathrm{R}}}$ is in proportion to α_R and thus in proportion to the mean electric field E.

The extracted spin-orbit relaxation length L_{SO} from the measured magnetoconductance data in our experiments comprise contributions from comprehensive spin relaxation processes induced by all kinds of SOIs (i.e., Rashba SOI, Dresselhaus SOI and other high-order kinds). It is naturally a hypothesis that the Rashba SOI induced spin precession process is the major cause for the WAL characteristics observed in our magnetoconductance measurements. Thus, the spin procession induced relaxation time τ_{SO} caused by all SOIs could be written as $\frac{1}{\tau_{\mathrm{SO}}} = \frac{1}{\tau_{\mathrm{R}}} + \cdots$, where τ_{R} is the spin relaxation time cause by the Rashba SOI. As a consequence, we have $\frac{1}{{L_{\mathrm{SO}}}^2} = \frac{1}{{L_{\mathrm{R}}}^2} + \cdots$ and thus expect to see that $\frac{1}{{L_{\mathrm{SO}}}^2} = \left(\frac{m^* r_{\mathrm{R}}}{\hbar^2}\right)^2 E^2 + C_0$ in the InSb nanolayer in our device, where C_0 is a constant by assuming that the Elliot-Yafet term, Dresselhaus SOI term and all other high-order terms are electric field independent. To see this, we plot in Fig. 4, the extracted $\frac{1}{{L_{\mathrm{SO}}}^2}$ as a function of E^2 at carrier densities of $n = 7.2 \times 10^{11}$ cm^{-2} and 4.3×10^{11} cm^{-2}. The red and blue dashed lines in the figure show the linear fits to the data at the two different carrier densities, namely different Fermi levels. As shown in Fig. 4, at both carrier densities, $\frac{1}{{L_{\mathrm{SO}}}^2}$ displays a good linear dependence on E^2. The slopes $\kappa = \left(\frac{m^* r_{\mathrm{R}}}{\hbar^2}\right)^2$ of the fitting lines are 0.613 V^{-2} at $n = 7.2 \times 10^{11}$ cm^{-2} and 0.41 V^{-2} at $n = 4.3 \times 10^{11}$ cm^{-2}. This result supports our above assumption that the Rashba SOI induced spin precession process is the major cause for the observed

gate voltage tunable WAL characteristics. The intercepts of the two fitting lines and the vertical axis are nearly the same and are very close to a value of 8 μm^{-2}, which gives C_0 =8 μm^{-2} and represents all other field-independent contributions including the one from the Dresselhaus SOI. The Fermi level dependent prefactors r_{R} can be obtained from the extracted slopes κ using the relation $r_{\mathrm{R}} = \frac{\hbar^2}{m^*} \cdot \sqrt{\kappa}$. The results are $r_{\mathrm{R}} =$ 4.26 e·nm^2 at $n =$ 7.2×10^{11} cm^{-2} and $r_{\mathrm{R}} =$ 3.48 e·nm^2 at $n =$ 4.3×10^{11} cm^{-2}.

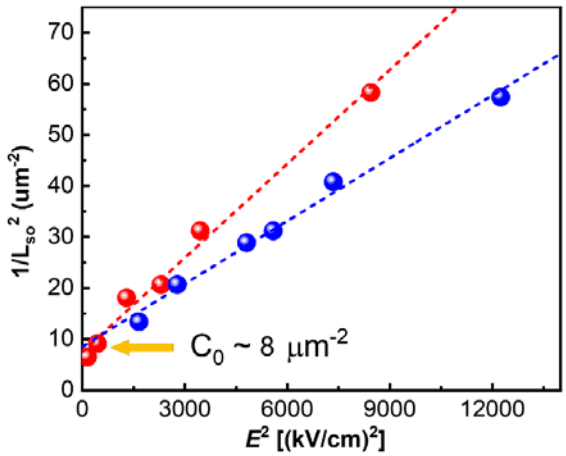

Figure 4. Extracted $\frac{1}{l_{\mathrm{SO}}{}^2}$ versus calculated mean field strength E^2 in the InSb nanolayer of the dual-gate device. Red and blue dots are the data points obtained at sheet carrier densities $n =$ 7.2×10^{11} cm^{-2} and 4.3×10^{11} cm^{-2}, respectively. Red and blue dashed lines are the linear fits to the data. The two fitting lines intersect the vertical axis at nearly the same value of C_0~8 μm^{-2} as marked by a yellow arrow.

Supplementary Note V. Dual-gate voltage dependent measurements of the magnetoconductance along the constant conductance contour lines of ~1.1 and ~2.6 e^2/h

The dual-gate voltage dependent measurements of the magnetoconductance and the characteristics transport lengths have also been performed for the InSb nanosheet at two lower carrier densities, i.e., along the constant conductance contour lines of ~1.1 and ~2.6 e^2/h. Figure 5 summarizes the measurements, where Figs. 5(a) and 5(b) show the results along the constant conductance contour line of ~2.6 e^2/h, while Figs. 5(c) and 5(d) show the results along the constant conductance contour line of ~1.1 e^2/h. It is seen that similar dual-gate voltage dependences of the transport lengths L_φ, L_{so}, and L_{e} as observed in Fig. 3 of the main article are obtained. In particular, the

spin-orbit length L_{SO} is seen to be efficiently controlled via the dual-gate voltage V_{D} at both constant conductance values. These data, together with those shown in Fig. 3 of the main article, demonstrate that the SOI in the InSb nanosheet in a dual-gate structure can be efficiently tuned by a voltage applied to the dual gate at largely different but fixed carrier densities of the nanosheet.

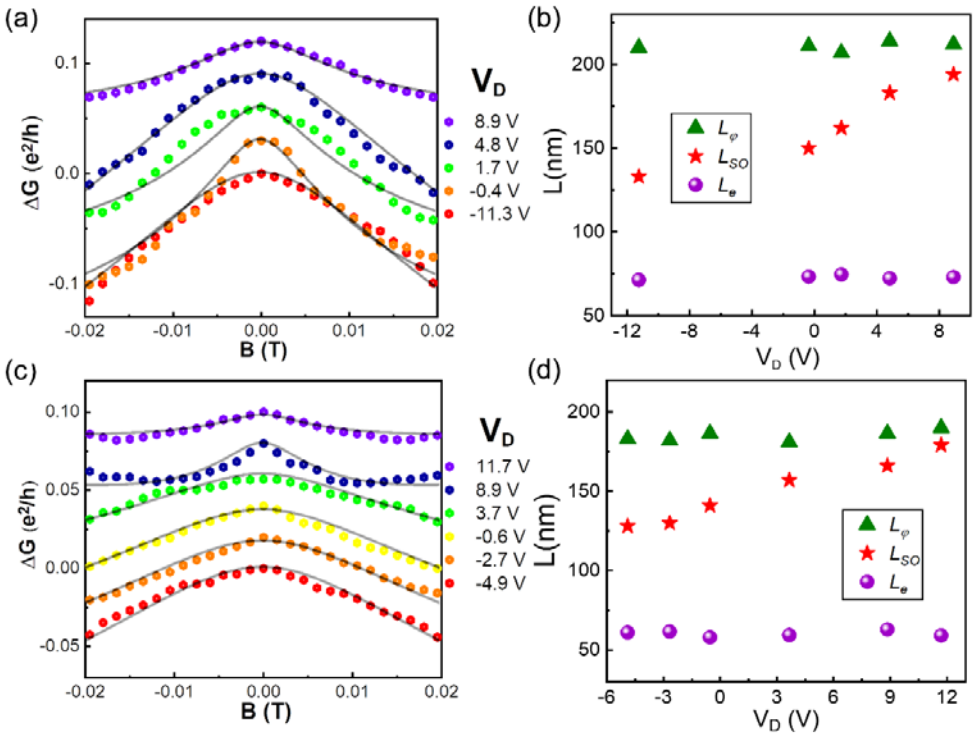

Figure 5. (a) Low-field magnetoconductance ΔG measured for the device at a constant conductance value of ~ 2.6 e^2/h and temperature T = 1.9 K at various values of the voltage $V_{\mathrm{D}} = V_{\mathrm{TG}} - V_{\mathrm{BG}}$ applied over the dual gate. The bottom trace shows the magnetoconductance data measured at $V_{\mathrm{D}} = -11.3$ V and all other measured magnetoconductance traces are successively vertically offset for clarity. The black solid lines are the theoretical fits of the experimental data to the HLN equation [Eq. (1) in the main article]. (b) Phase coherence length L_{φ}, spin-orbit length L_{SO}, and mean free path L_{e} extracted from the fits in (a) as a function of V_{D}. (c) The same as (a) but measured for the device at a constant conductance value of ~1.1 e^2/h. Here, the bottom trace shows the magnetoconductance data measured at $V_D = -4.9$ V and all other measured magnetoconductance traces are again successively vertically offset for clarity. (d) Phase coherence length L_{φ}, spin-orbit length L_{SO}, and mean free path L_{e} extracted from the fits in (c) as a function of V_{D}.

References

1. Knap. W. et al. Weak antilocalization and spin precession in quantum wells. Phys. Rev. B 53, 3912 (1996).
2. Winkler, R. Spin–Orbit Coupling Effects in Two-Dimensional Electron and Hole Systems (Springer Tracts in Modern Physics, Vol. 191, Springer, 2003).
3. Dresselhaus, G. Spin-orbit coupling effects in zinc blende structures. *Phys. Rev.* **100,** 580–586 (1955).
4. Bychkov, Y. A. & Rashba, E. Oscillatory effects and the magnetic susceptibility of carriers in inversion layers. *J. Phys. C* **17**, 6039–6045 (1984).
5. Bychkov, Y. A. & Rashba, E. *JETP lett*, **39**, 78 (1984).
6. Lommer, G., F. Malcher, and U. Rossler. Reduced g factor of subband Landau levels in AlGaAs/GaAs heterostructures. *Phys. Rev. B* **32**. 6965 (1985).
7. Lommer, G., F. Malcher, and U. Rossler. Spin splitting in semiconductor heterostructures for B→ 0. *Phys. Rev. B* **60**. 728 (1988).